Artificial neural network approach for turbulence models: A local framework

Chenyue Xie [1,*] Xiangming Xiong [1] and Jianchun Wang [2,†]

[1]*Program in Applied and Computational Mathematics, Princeton University,
Princeton, New Jersey 08544, USA*
[2]*Department of Mechanics and Aerospace Engineering, Southern University of Science
and Technology, Shenzhen 518055, People's Republic of China*

A local artificial neural network (LANN) framework is developed for turbulence modeling. The Reynolds-averaged Navier-Stokes (RANS) unclosed terms are reconstructed by the artificial neural network based on the local coordinate system which is orthogonal to the curved walls. We verify the proposed model in the flows over periodic hills. The correlation coefficients of the RANS unclosed terms predicted by the LANN model can be made larger than 0.96 in an *a priori* analysis, and the relative error of the unclosed terms can be made smaller than 18%. In an *a posteriori* analysis, detailed comparisons are made on the results of RANS simulations using the LANN, global artificial neural network (GANN), Spalart-Allmaras (SA), and shear stress transport (SST) k-ω models. It is shown that the LANN model performs better than the GANN, SA, and SST k-ω models in the prediction of the average velocity, wall-shear stress, and average pressure, which gives the results that are essentially indistinguishable from the direct numerical simulation data. The LANN model trained at low Reynolds number, Re = 2800, can be directly applied to the cases of high Reynolds numbers, Re = 5600, 10 595, 19 000, and 37 000, with accurate predictions. Furthermore, the LANN model is verified for flows over periodic hills with varying slopes. These results suggest that the LANN framework has a great potential to be applied to complex turbulent flows with curved walls.

I. INTRODUCTION

The Reynolds-averaged Navier-Stokes (RANS) simulation has been widely applied to study complex turbulent flows in industrial applications, combustion, astrophysics, and engineering problems for its low computing requirements [1–3], which can be derived by time averaging of the Navier-Stokes equations [2]. Since the pioneering works of Reynolds by decomposing the instantaneous quantity into its time-averaged and fluctuating quantities [4], a series of model-driven approaches has been proposed to develop RANS models. These include the eddy viscosity models [5,6], the Spalart-Allmaras model [7], the k-ϵ model [8–11], the k-ω model [12–14], the Reynolds stress model (RSM) [15], etc. [2].

Recently, data-driven techniques have been incorporated into turbulence models [16–46]. The discrepancies in the Reynolds stress anisotropy tensor are reconstructed by supervised learning [16]. Duraisamy *et al.* proposed a data-driven approach to the modeling of turbulence with enforcing consistency between the data and the model [17,18]. Ling *et al.* developed the neural network architectures embedded invariance properties in RANS simulations [22]. A physics-informed

*Corresponding author: chenyuex@princeton.edu
†wangjc@sustech.edu.cn

Bayesian framework for quantifying and reducing model-form uncertainties in RANS simulations has been proposed by Xiao *et al.* [24]. Reynolds stress modeling discrepancies can be reconstructed by a physics-informed machine-learning approach [27]. A physics-based implicit treatment was proposed to model Reynolds stress by using machine-learning techniques [33]. Wu *et al.* proposed a metric to quantitatively assess the conditioning of RANS equations with data-driven Reynolds stress closures [36]. Furthermore, the recent progresses on data-driven turbulence models have been summarized by Duraisamy *et al.* [41].

In this paper, we propose a local artificial neural network (LANN) framework for reconstructing the RANS unclosed terms in the local coordinate system orthogonal to the curved wall. We find that the Reynolds unclosed terms predicted by the LANN model exhibit high accuracy in the *a priori* analysis for flows over periodic hills. We also study the accuracy of the proposed LANN model in the *a posteriori* tests by examining the average velocity, wall-shear stress, and average pressure. These tests suggest that the LANN model is a very attractive approach for developing models of RANS unclosed terms in complex turbulent flows with curved walls.

This paper is organized as follows. Section II briefly describes the governing equations and computational method. Section III discusses the direct numerical simulation (DNS) database of compressible flows over periodic hills. Section IV introduces the LANN model for the reconstruction of RANS unclosed terms from the averaged flow fields. Section V presents both *a priori* and *a posteriori* results of the LANN model. Some discussions on the proposed LANN models are presented in Sec. VI. Conclusions are drawn in Sec. VII.

II. GOVERNING EQUATIONS AND NUMERICAL METHOD

The dimensionless Navier-Stokes equations for compressible turbulence of ideal gas in the conservation form are [47–51]

$$\frac{\partial \rho}{\partial t} + \frac{\partial(\rho u_j)}{\partial x_j} = 0, \tag{1}$$

$$\frac{\partial(\rho u_i)}{\partial t} + \frac{\partial[\rho u_i u_j + p\delta_{ij}]}{\partial x_j} = \frac{1}{\mathrm{Re}}\frac{\partial \sigma_{ij}}{\partial x_j}, \tag{2}$$

$$\frac{\partial \mathcal{E}}{\partial t} + \frac{\partial[(\mathcal{E}+p)u_j]}{\partial x_j} = \frac{1}{\alpha}\frac{\partial}{\partial x_j}\left(\kappa\frac{\partial T}{\partial x_j}\right) + \frac{1}{\mathrm{Re}}\frac{\partial(\sigma_{ij}u_i)}{\partial x_j}, \tag{3}$$

$$p = \rho T/(\gamma \mathrm{Ma}^2), \tag{4}$$

where u_i is the ith velocity component ($i = 1, 2, 3$), p is the pressure, ρ is the density, and T is the temperature. The viscous stress is defined by $\sigma_{ij} = 2\mu S_{ij} - \frac{2}{3}\mu\delta_{ij}S_{kk}$, where $S_{ij} = \frac{1}{2}(\partial u_i/\partial x_j + \partial u_j/\partial x_i)$ is the strain rate tensor. The molecular viscosity $\mu = \frac{T^{3/2(1+S)}}{T+S}$ ($S = 110.4K/T_f$) is determined from Sutherland's law [52], and the thermal conductivity κ is then calculated from the molecular viscosity with the constant Prandtl number assumption. The total energy per unit volume $\mathcal{E}$ is defined by $\mathcal{E} = \frac{p}{\gamma-1} + \frac{1}{2}\rho(u_j u_j)$.

The hydrodynamic and thermodynamic variables in Eqs. (1)–(4) are normalized by a set of reference variables: the reference velocity U_f, temperature T_f, length L_f, density ρ_f, energy per unit volume $\rho_f U_f^2$, viscosity μ_f, thermal conductivity κ_f, and pressure $p_f = \rho_f U_f^2$. There are three reference governing parameters: the reference Reynolds number, $\mathrm{Re} \equiv \rho_f U_f L_f/\mu_f$, the reference Mach number, $\mathrm{Ma} = U_f/c_f$, and the reference Prandtl number, $\mathrm{Pr} \equiv \mu_f C_p/\kappa_f$. The speed of sound is defined by $c_f \equiv \sqrt{\gamma R T_f}$, where $\gamma \equiv C_p/C_v$ is the ratio of specific heat at constant pressure C_p to that at constant volume C_v and is assumed to be equal to 1.4. Moreover, $R \equiv C_p - C_v$ is the specific gas constant. The parameter Pr is assumed to be equal to 0.7. The parameter α is given by $\alpha \equiv \mathrm{Pr}\,\mathrm{Re}(\gamma - 1)\mathrm{Ma}^2$.

The RANS equations govern the dynamics of the mean scales, which can be obtained by projecting the physical variables into the time-averaged variables by a Reynolds operation $\bar{f}(\mathbf{x}) =$

$\lim_{T_R \to \infty} \frac{1}{T_R} \int_{t_0}^{t_0+T_R} f(\mathbf{x}, t) \, dt$, where $\bar{f}$ denotes a time-averaged variable and T_R is the integration time[4]. Favre filtering (mass-weighted filtering, $\tilde{f} = \overline{\rho f}/\bar{\rho}$) [53] is used to avoid additional RANS unclosed terms and simplify the treatments in the equation of conservation of mass in compressible flows. The Favre average obeys the following decomposition rules: $f = \bar{f} + f'$ and $f = \tilde{f} + f''$.

The dimensionless compressible governing equations for the time-averaged variables can be expressed as follows:

$$\frac{\partial \bar{\rho}}{\partial t} + \frac{\partial (\bar{\rho} \tilde{u}_j)}{\partial x_j} = 0, \tag{5}$$

$$\frac{\partial (\bar{\rho} \tilde{u}_i)}{\partial t} + \frac{\partial (\bar{\rho} \tilde{u}_i \tilde{u}_j + \bar{p} \delta_{ij})}{\partial x_j} - \frac{1}{\mathrm{Re}} \frac{\partial \tilde{\sigma}_{ij}}{\partial x_j} = \frac{\partial \tau_{ij}}{\partial x_j}, \tag{6}$$

$$\frac{\partial \tilde{\mathcal{E}}}{\partial t} + \frac{\partial [(\tilde{\mathcal{E}} + \bar{p}) \tilde{u}_j]}{\partial x_j} - \frac{1}{\mathrm{Re}} \frac{\partial (\tilde{\sigma}_{ij} \tilde{u}_i)}{\partial x_j} - \frac{1}{\alpha} \frac{\partial}{\partial x_j} \left(\tilde{\kappa} \frac{\tilde{T}}{x_j} \right) = \frac{\partial C_p Q_i}{\partial x_i} + \frac{\partial J_i}{\partial x_i}, \tag{7}$$

$$\bar{p} = \bar{\rho} \tilde{T}/(\gamma \mathrm{Ma}^2), \tag{8}$$

where the time-averaged total energy $\tilde{\mathcal{E}}$ is defined by $\tilde{\mathcal{E}} = \frac{\bar{p}}{\gamma - 1} + \frac{1}{2} \bar{\rho} (\tilde{u}_j \tilde{u}_j)$, the time-averaged viscous stress is $\tilde{\sigma}_{ij} = 2\tilde{\mu} \tilde{S}_{ij} - \frac{2}{3} \tilde{\mu} \delta_{ij} \tilde{S}_{kk}$, where $\tilde{S}_{ij} = \frac{1}{2}(\partial \tilde{u}_i/\partial x_j + \partial \tilde{u}_j/\partial x_i)$, and $\tilde{\mu}$ is calculated from Sutherland's law.

The RANS unclosed terms appearing on the right-hand sides of Eqs. (5)–(8) are defined as

$$\tau_{ij} = -\bar{\rho} \widetilde{u_i'' u_j''}, \quad Q_j = -\bar{\rho} \widetilde{u_j'' T''}, \tag{9}$$

where τ_{ij} is the Reynolds stress, Q_j is the turbulent heat flux, and J_i is the triple correlation term $J_i = -\frac{1}{2} \bar{\rho} (\widetilde{u_j u_j u_i} - \widetilde{u_j u_j} \tilde{u}_i) \approx \tau_{ij} \tilde{u}_j$ [54,55].

In this paper, we model the Reynolds stress τ_{ij} and turbulent heat flux Q_j, and neglect other unclosed terms. Meanwhile, we assume that the kinematic viscosity satisfies the following condition: $\overline{\sigma_{ij}} = \overline{2\rho \nu (S_{ij} - \frac{1}{3}\delta_{ij} S_{kk})} = 2\bar{\rho}\nu(\widetilde{S_{ij}} - \frac{1}{3}\delta_{ij}\widetilde{S_{kk}})$, where ν is the kinematic viscosity, and the term $\frac{1}{\mathrm{Re}} \frac{\partial \overline{\sigma_{ij}} - \tilde{\sigma}_{ij}}{\partial x_j}$ would not appear in the filtered momentum equation.

III. DNS DATABASE OF COMPRESSIBLE TURBULENCE

The DNS data of the compressible flows over the periodic hills (the baseline geometry of a periodic hill is depicted by piecewise cubic polynomials [56,57]) are obtained from direct numerical simulation with the high-order finite difference Navier-Stokes solver OpenCFD-SC [48,58]. A sixth-order compact finite difference scheme is used for space discretization and a third-order Runge-Kutta scheme is used for time integration [48,59]. No-slip velocity and adiabatic conditions are imposed on the upper and lower walls for the velocity and temperature, respectively. We implement periodic boundary conditions in the streamwise x and spanwise z directions. A body-fitted curvilinear grid system is used in all of the simulations [60]. The flows are driven by a body force $F(t)$ in the streamwise direction, which is a function of time only, and maintainthat the average mass flux remains constant at every time step [50,61]: $\frac{\partial}{\partial t} \int_{\mathrm{vol}} \rho u \, dv = 0$.

The periodic hill channel flow configuration is shown in Fig. 1 [50,51,57,61–63]. The lengths are nondimensionalized by the height of the hill, h. The dimensionless computational domain is $(0, L_x) \times 0, L_y \times (0, L_z)$, where $L_x = 9$, $L_y = 3.035$, and $L_z = 4.5$. The cross-section Reynolds number over the hill crest is defined as $\mathrm{Re}_S = \int_S (\rho u_1)|_{x=0} dS h/(\int_S dS \mu_{\mathrm{wall}})$, where h is the hill height. The volumetric Reynolds number is $\mathrm{Re}_v = \int_V \rho u_1 dV h/(\int_V dV \mu_{\mathrm{wall}})$. A relationship between Re_S and Re_v is $\mathrm{Re}_v = 0.72 \mathrm{Re}_S$[55,61]. The wall temperature is fixed at 300 K. We present the DNS results at the Reynolds number Re ranging from 2800 to 10 595 and Mach number Ma = 0.2 ($\mathrm{Ma} = \int_S (u_1)|_{x=0} dS/(\int_S dS c_{\mathrm{wall}})$) with the grid resolution of $256 \times 129 \times 128$.

The instantaneous streamwise velocity field at $z = 0$ is shown in Fig. 2(a). The flow field is divided into two regions: the reverse flow with $u_1 < 0$ and the forward flow with $u_1 > 0$. Meanwhile,
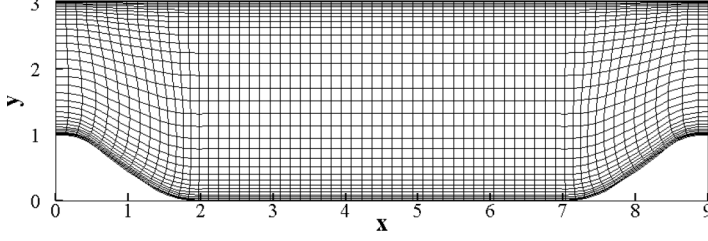
FIG. 1. The configuration of the flow over a periodic hill: every fourth curvilinear grid line is shown.

the statistical average quantities are obtained by averaging the quantities in the spanwise direction and temporally for 200 flow-through times. The contour of the mean streamwise velocity and the streamlines are displayed in Fig. 2(b). Back-flow and separation occur behind the first hill. The separation and reattachment points are $x_{sep} = 0.227$ and $x_{reatt} = 5.34$, respectively [50,61,62].

The comparison of the mean streamwise and normal velocities $\tilde{u}_1$ and $\tilde{u}_2$ at 11 stations $x = 0$, 0.5, 1, 2, 3, 4, 5, 6, 7, 8, and 8.5 for Reynolds numbers Re = 2800, 5600, and 10 595 are shown in Fig. 3. $\tilde{u}_1$ and $\tilde{u}_2$ computed from the present simulations are in excellent agreement with the DNS results of Breuer et al. [50,62]. Figure 4 shows the Favre-averaged Reynolds stresses $\overline{\rho u_1'' u_1''}$ and $\overline{\rho u_1'' u_2''}$ at Re = 2800. It can be seen that the solved $\overline{\rho u_1'' u_1''}$ and $\overline{\rho u_1'' u_2''}$ by present simulation agree well with the results of Breuer et al. [50,62]. Furthermore, the averaged pressure distribution $\bar{p} - \bar{p}_{ave}$ ($\bar{p}_{ave} = \frac{1}{L_x} \int_0^{L_x} \bar{p}\, dx$) along the lower wall is shown in Fig. 5. The pressure from the present simulation is close to the previous DNS [62]. These comparisons validate the accuracy of the present direct numerical simulations.

IV. THE STRUCTURE OF THE LANN MODEL

A fully connected artificial neural network (ANN) is used to reconstruct the nonlinear relation between average input features and RANS unclosed terms τ_{ij} and Q_j. The network structure of the ANN is shown in Fig. 6 [64–66]. Neurons in layer l of ANN receive signals X_j^{l-1} from layer $l-1$ and process them with a series of linear or nonlinear mathematical operations, and then send signals X_i^l to neurons in layer $l+1$ [67–69]. The transfer function is calculated as

$$X_i^l = \sigma\left(s_i^l + b_i^l\right), \tag{10}$$

$$s_i^l = \sum_j W_{ij}^l X_j^{l-1}, \tag{11}$$

where W_{ij}^l, b_i^l, and σ are the weight, bias parameter, and activation function, respectively. We train the ANN to update the weights and bias parameters so that the final output X^O approximates well the RANS unclosed terms τ_{ij} and Q_j. Five ANNs are trained to predict each independent component of τ_{ij} and Q_j separately.
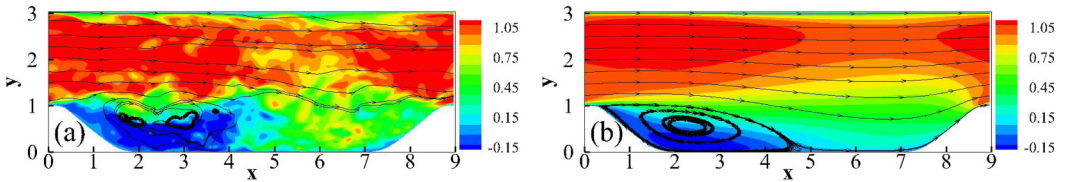

FIG. 2. Contours of the streamwise velocity field at Re = 2800: (a) the instantaneous streamwise velocity field in the (x-y) plane at $z = 0$ and (b) the mean streamwise velocity $\tilde{u}_1$ and the streamlines.
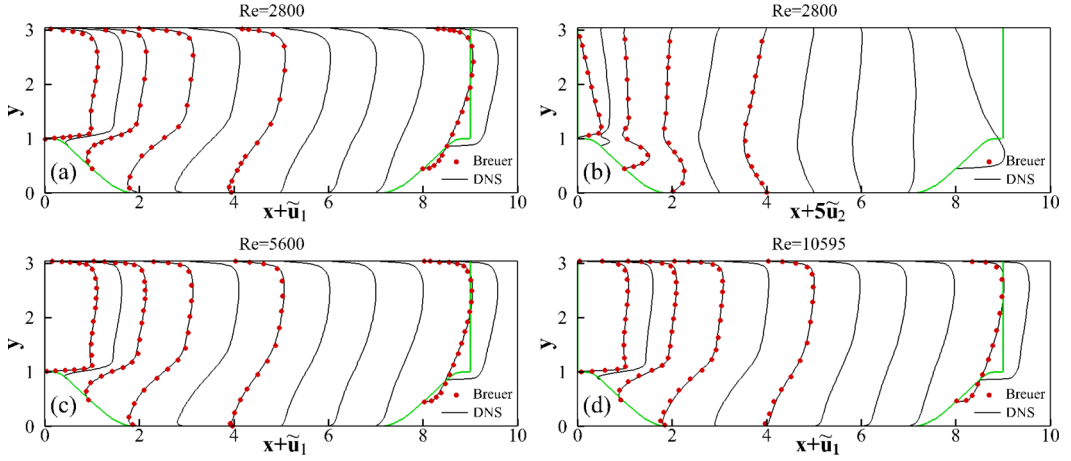
FIG. 3. Profiles of the mean streamwise and normal velocities, $\tilde{u}_1$ and $\tilde{u}_2$, at different stations $x = 0, 0.5,$ 1, 2, 3, 4, 5, 6, 7, 8, and 8.5 with Re = 2800, 5600, and 10 595: (a) $\tilde{u}_1$ at Re = 2800, (b) $\tilde{u}_2$ at Re = 2800, (c) $\tilde{u}_1$ at Re = 5600, and (d) $\tilde{u}_1$ at Re = 10 595.

In this research, the fully connected ANN contains four layers of neurons ($M : 64 : 32 : 1$) between the set of inputs and targets. The input layer has M neurons, while the output layer consists of a single neuron. Two hidden layers are activated by the Leaky-Relu activation
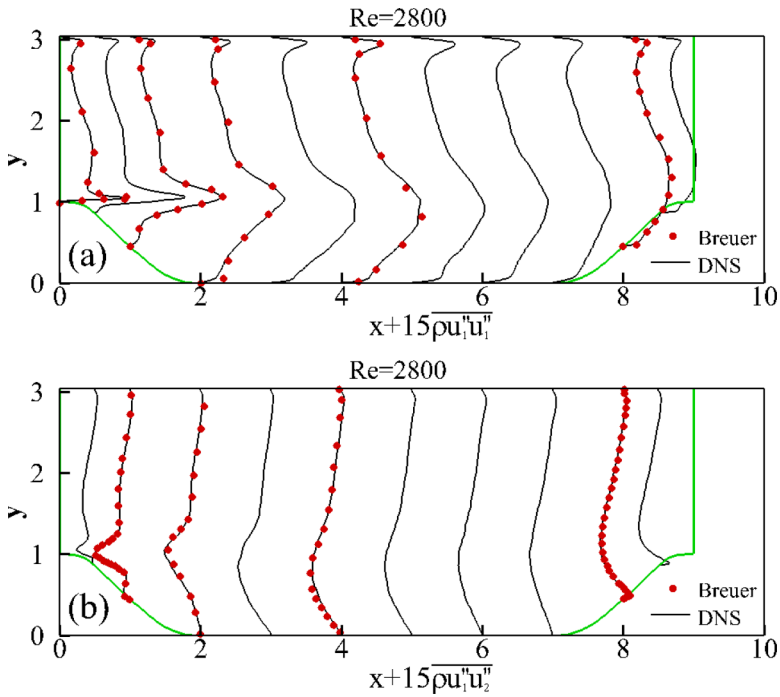

FIG. 4. Profiles of the Favre-averaged Reynolds stresses $\overline{\rho u_1'' u_1''}$ and $\overline{\rho u_1' u_2'}$ at different stations with Re = 2800.
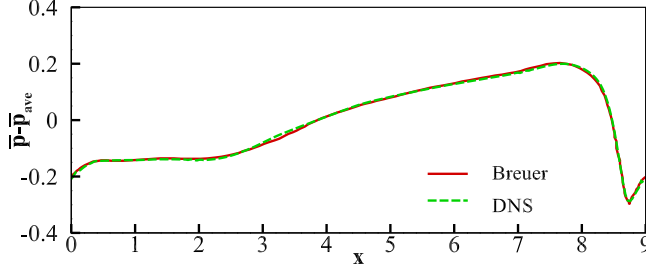
FIG. 5. The averaged pressure distribution $\bar{p} - \bar{p}_{\mathrm{ave}}$ along the lower wall for Re = 2800.

function:

$$\sigma(a) = \begin{cases} a & \text{if } a > 0 \\ 0.2a & \text{if } a \leqslant 0. \end{cases} \tag{12}$$

Meanwhile, linear activation $\sigma(a) = a$ is used to the output layer. The loss function is defined by the difference between the output X^O and the RANS unclosed terms from DNS ($\langle (X^O - \tau_{ij})^2 \rangle$ or $\langle (X^O - Q_j)^2 \rangle$), where $\langle \rangle$ represents the average over the entire domain [64]. The loss function is minimized by the back-propagation method with Adam optimizer (learning rate is 0.001) [70].

The proper choice of input variables for flows over periodic hills with varying slopes is important for the present ANN architecture to model the Reynolds stress τ_{ij} and the turbulent heat flux Q_j accurately. As shown in the previous work [41], the first-order derivatives of averaged velocities have been used to establish a functional relation between $\{\frac{\partial \bar{u}_i}{\partial x_j}, d\}$ (d is the nearest distance from the walls) and the RANS unclosed terms [41].

In the RANS simulations of flows over periodic hills with varying slopes, the RANS unclosed terms have been predicted by machine-learning models, where the input features contain the first-order derivatives of the mean velocity and temperature in the global reference frame [41]. Because the angle between the local wall-normal direction and the global y direction varies with the spatial position, it is difficult to extend the trained machine-learning model to flows over periodic hills with varying slopes in the global reference frame, which makes it useless for other flows with general boundaries. In order to optimize the input features while maintaining accuracy and generality, we proposed the LANN model, which reconstructs the nonlinear function of the input features and RANS unclosed terms τ_{ij} and Q_j in the local coordinate system orthogonal to the nearest wall
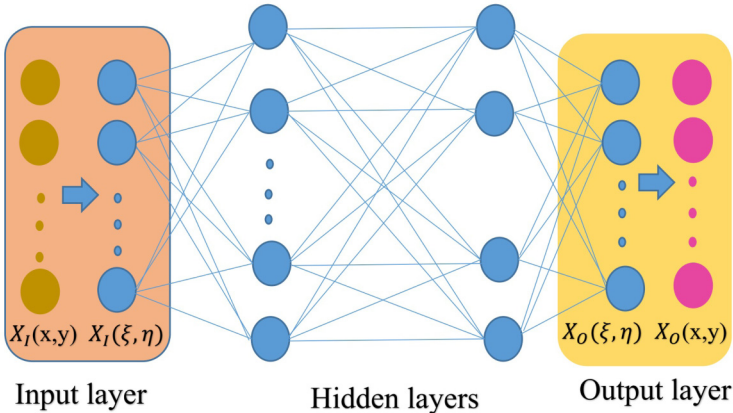

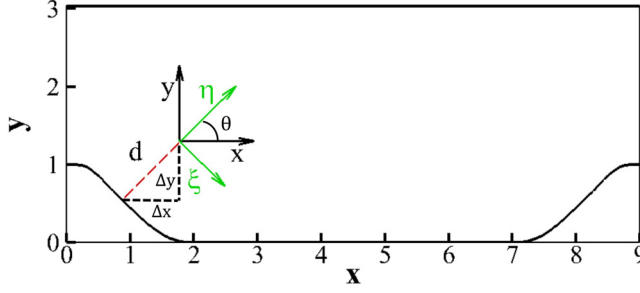FIG. 6. Schematic diagram of the ANN's structure.

FIG. 7. Transformation between the global and local reference frames in the flow over a periodic hill.

as shown in Fig. 7. The LANN model guarantees that the nearest distance between the present point and the wall (d) can be measured along the η direction of the local coordinate system, which is general for flows over periodic hills with varying slopes. A set of input variables and output variables of different ANNs is shown in Table I. As shown in Fig. 6, the input and output features $X_I(x, y), X_O(x, y)$ in the global reference frame are transformed to $X_I(\xi, \eta), X_O(\xi, \eta)$ in the local reference frame for flows over periodic hills:

$$\begin{pmatrix} \frac{\partial \tilde{u}_\xi}{\partial \xi} & \frac{\partial \tilde{u}_\xi}{\partial \eta} \\ \frac{\partial \tilde{u}_\eta}{\partial \xi} & \frac{\partial \tilde{u}_\eta}{\partial \eta} \end{pmatrix} = A \begin{pmatrix} \frac{\partial \tilde{u}_x}{\partial x} & \frac{\partial \tilde{u}_x}{\partial y} \\ \frac{\partial \tilde{u}_y}{\partial x} & \frac{\partial \tilde{u}_y}{\partial y} \end{pmatrix} A^T, \tag{13}$$

$$\begin{pmatrix} \frac{\partial \tilde{T}}{\partial \xi} & \frac{\partial \tilde{T}}{\partial \eta} \end{pmatrix} = \begin{pmatrix} \frac{\partial \tilde{T}}{\partial x} & \frac{\partial \tilde{T}}{\partial y} \end{pmatrix} A^T, \tag{14}$$

$$\begin{pmatrix} \tau_{\xi\xi} & \tau_{\xi\eta} \\ \tau_{\eta\xi} & \tau_{\eta\eta} \end{pmatrix} = A \begin{pmatrix} \tau_{xx} & \tau_{xy} \\ \tau_{yx} & \tau_{yy} \end{pmatrix} A^T, \tag{15}$$

$$(Q_{\xi T} \quad Q_{\eta T}) = (Q_{xT} \quad Q_{yT}) A^T, \tag{16}$$

where $A = \begin{pmatrix} \sin(\theta) & -\cos(\theta) \\ \cos(\theta) & \sin(\theta) \end{pmatrix}$, $\cos(\theta) = \frac{\Delta x}{r}$, $\sin(\theta) = \frac{\Delta y}{r}$, and $r = \sqrt{\Delta x^2 + \Delta y^2}$.

In order to increase the robustness of the ANN training, the first-order derivatives of the mean velocity and temperature in X_I are normalized by their root mean square (rms) values, which is similar to the previous data-driven strategies [20,24,27,30,66,69]:

$$Z_I = X_I / X_I^{\text{rms}}. \tag{17}$$

Besides, we suppress overfitting with a cross validation. The performance of the model is estimated by the test data. In this research, the inputs and outputs of the LANN model are the mean flow features and the RANS unclosed terms τ_{ij}, Q_j, respectively, which are obtained from the DNS data. The three-dimensional (3D) DNS data are generated using $256 \times 129 \times 128$ degrees of freedom while the two-dimensional (2D) RANS is performed at the grid resolutions of 256×129 and 128×65. Finally, the network is trained by the Adam algorithm [70] with early stopping (if validation errors did not decrease or improve for 10 epochs, the training would exit with the best model corresponding to the lowest validation loss until then) [65]. The learning rate and batch size

TABLE I. Set of inputs and outputs for the ANNs.

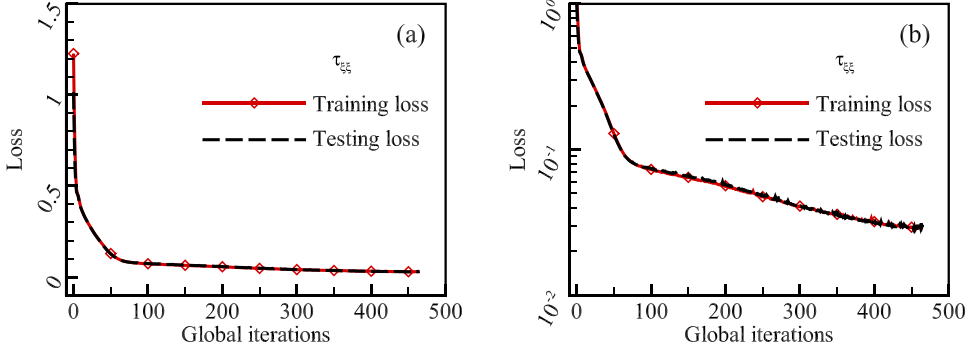| ANN	Inputs	Outputs
ANN1	$\frac{\partial \tilde{u}_\xi}{\partial \xi}, \frac{\partial \tilde{u}_\xi}{\partial \eta}, \frac{\partial \tilde{u}_\eta}{\partial \xi}, \frac{\partial \tilde{u}_\eta}{\partial \eta}, \bar{\rho}, d, \bar{\mu}$	$\tau_{\xi\xi}, \tau_{\xi\eta}, \tau_{\eta\xi}, \tau_{\eta\eta}$
ANN2	$\frac{\partial \tilde{u}_\xi}{\partial \xi}, \frac{\partial \tilde{u}_\xi}{\partial \eta}, \frac{\partial \tilde{u}_\eta}{\partial \xi}, \frac{\partial \tilde{u}_\eta}{\partial \eta}, \frac{\partial \tilde{T}}{\partial \xi}, \frac{\partial \tilde{T}}{\partial \eta}, \bar{\rho}, d, \bar{\mu}$	Q_ξ, Q_η

FIG. 8. Learning curves of the proposed LANN model of the unclosed Reynolds stress $\tau_{\xi\xi}$: (a) standard axes and (b) semilogarithmic axes.

of the ANN are 0.001 and 1000, respectively. The total data for ANN training are 32 639 grid points at Re = 2800; 70% of data are for training, and the remaining 30% are for testing. The training and testing losses show similar behavior and correlate closely after 100 global iterations as shown in Fig. 8, which implies that the learning process is reasonable.

V. TEST RESULTS OF THE LANN MODEL

In this section, we conduct both *a priori* and *a posteriori* tests to evaluate the performance of the LANN model for flows over periodic hills. In the *a priori* tests, the turbulence models are directly computed from the DNS data as functions of the Reynolds averaged gradients of velocity and temperature. The turbulence models' performance is evaluated by comparing the Reynolds stress and turbulent heat flux with the corresponding unclosed terms extracted from DNS. In the *a posteriori* tests, the RANS simulation results by using different RANS models are compared with the true unclosed terms computed from the DNS. The LANN model trained at Re = 2800 is used to produce reliable and repeatable predictions at Re = 2800, 5600, 10 595, 19 000, and 37 000. We calculated the correlation coefficients and relative errors of the predicted RANS unclosed terms τ_{ij} and Q_j in the *a priori* test. In the *a posteriori* test, results of the RANS simulations with the LANN model are compared with the Spalart-Allmaras (SA) and shear stress transport (SST) k-ω models and the DNS database. It is shown that the RANS simulations with the proposed LANN model can predict the statistics of the averaged DNS data with high accuracy.

A. A priori tests

We evaluate the performance of the LANN model by calculating the correlation coefficient $C(R)$ and the relative error $E_r(R)$ of τ_{ij} and Q_j. $C(R)$ and $E_r(R)$ are defined, respectively, by

$$C(R) = \frac{\langle (R - \langle R \rangle)(R^{\text{model}} - \langle R^{\text{model}} \rangle) \rangle}{(\langle (R - \langle R \rangle)^2 \rangle \langle (R^{\text{model}} - \langle R^{\text{model}} \rangle)^2 \rangle)^{1/2}}, \tag{18}$$

$$E_r(R) = \frac{\sqrt{\langle (R - R^{\text{model}})^2 \rangle}}{\sqrt{\langle R^2 \rangle}}, \tag{19}$$

where $\langle \cdot \rangle$ denotes averaging over the volume. Table II shows the correlation coefficients and relative errors of $\tau_{\xi\eta}$ and Q_ξ in the local reference frame for the LANN model in both training and testing sets at Re = 2800. The difference between the results of training and testing sets is small, which implies that the training process of ANN is not overfitting. The correlation coefficients are larger than 0.96, and the relative errors are less than 0.18 for the LANN model.

TABLE II. Correlation coefficient (C) and relative error (E_r) of $\tau_{\xi\xi}$, $\tau_{\xi\eta}$, $\tau_{\eta\eta}$, $Q_{\xi T}$, and $Q_{\eta T}$ for the LANN model in the local reference frame at Re = 2800.

C	$\tau_{\xi\xi}$	$\tau_{\xi\eta}$	$\tau_{\eta\eta}$	Q_ξ	Q_η
Train	0.967	0.992	0.993	0.980	0.986
Test	0.966	0.992	0.993	0.979	0.987
E_r	$\tau_{\xi\xi}$	$\tau_{\xi\eta}$	$\tau_{\eta\eta}$	$Q_{\xi T}$	$Q_{\eta T}$
Train	0.140	0.111	0.082	0.177	0.164
Test	0.141	0.110	0.084	0.181	0.162

Eddy viscosity turbulence models have been widely used for aeronautical, meteorological, and other applications [2]. The Boussinesq hypothesis is applied to establish the relation between RANS unclosed terms and the first-order derivatives of mean velocity and temperature [5]. The traceless part of the Reynolds stress τ_{ij} is proportional to the product of the mean strain rate tensor $\tilde{S}_{ij}$ and the eddy viscosity μ_t. The Reynolds stress τ_{ij} and turbulent heat flux Q_j are [7] $\tau_{ij} = \mu_t \alpha_{ij} = -\mu_t(2\tilde{S}_{ij} - \frac{2}{3}\frac{\partial \tilde{u}_k}{\partial x_k})$, $Q_j = \mu_Q \beta_j = -\frac{C_p \mu_t}{Pr_T}\frac{\partial \tilde{T}}{\partial x_j}$, where $\alpha_{ij} = -2(\tilde{S}_{ij} - \frac{1}{3}\frac{\partial \tilde{u}_k}{\partial x_k})$, $\beta_j = -\frac{\partial \tilde{T}}{\partial x_j}$. The optimal eddy viscosities (OEVs) are defined as $\mu_t = \frac{\tau_{ij}\alpha_{ij}}{\alpha_{ij}\alpha_{ij}}$, $\mu_Q = \frac{Q_j\beta_j}{\beta_j\beta_j}$, which can minimize the discrepancy between the Reynolds stress τ_{ij} (or turbulent heat flux Q_j) and α_{ij} (or β_j) [33].
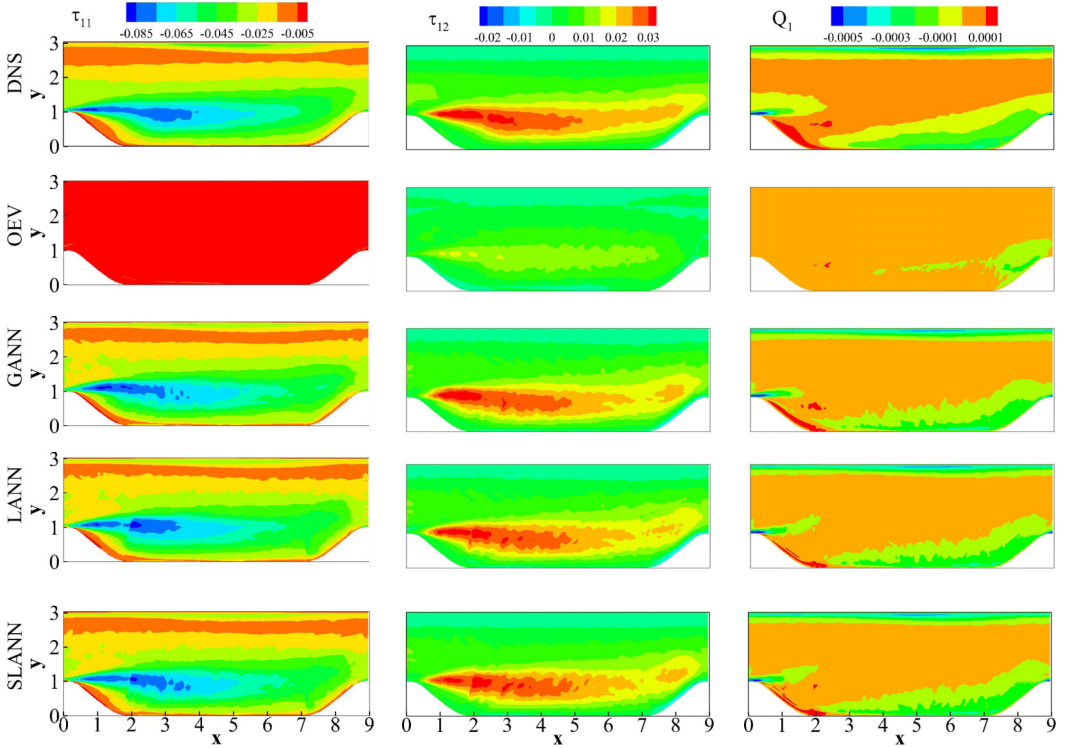

FIG. 9. The contours of the Reynolds stress components τ_{11}, τ_{12} and turbulent heat flux Q_1 predicted by different turbulence models at Re = 2800 with a grid resolution of 256×129 and $L_x = 9.0$. The rows show the predictions of the OEV, GANN, LANN, and SLANN models. The true DNS results are shown in the top row for comparison.
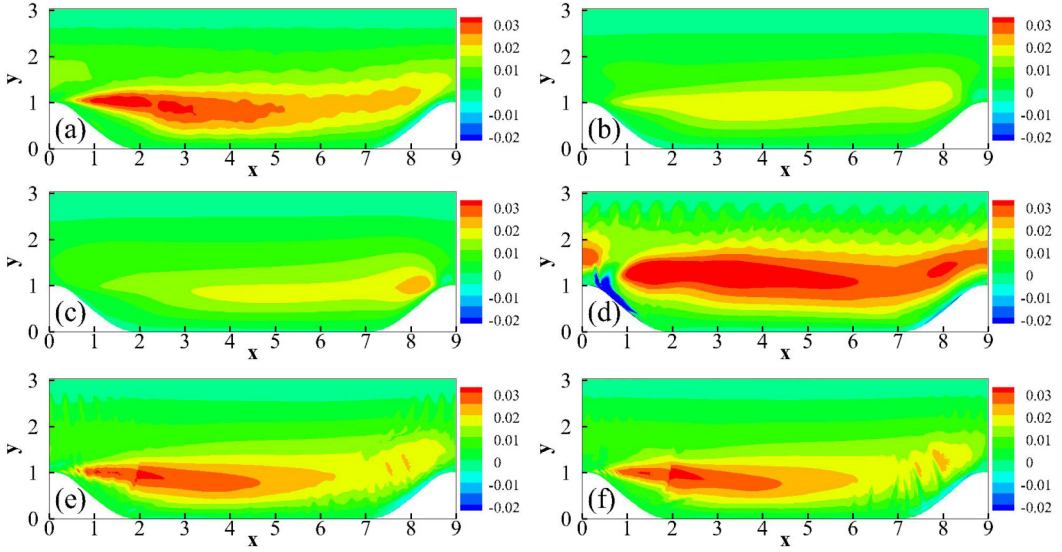
FIG. 10. The contours of the Reynolds shear stress τ_{12} of different turbulence models at Re $= 2800$ with a grid resolution of 256×129 and $L_x = 9.0$: (a) DNS, (b) SA model, (c) SST k-ω model, (d) GANN model, (e) LANN model, and (f) SLANN model.

In order to analyze the impact of the local reference frame vs the global reference frame on the results, the ANN trained in the global reference frame is abbreviated as GANN. The *a priori* results of different models are shown in Fig. 9. The OEV model cannot accurately reconstruct the Reynolds stress and turbulent heat flux. The GANN, LANN, and simultaneous local artificial neural network (SLANN) [the ANN with four (or two) outputs to represent and train all components
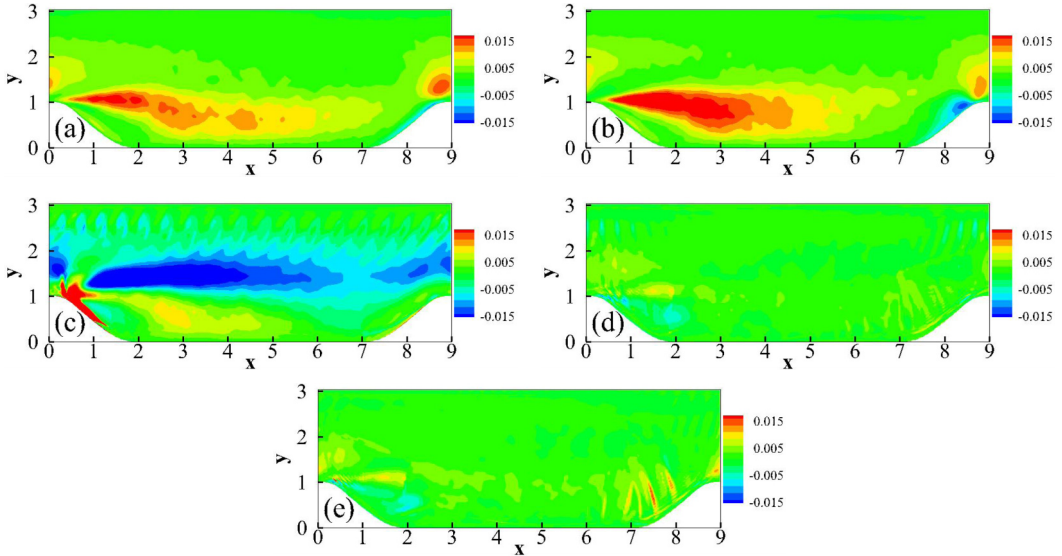

FIG. 11. The contours of the Reynolds shear stress error $\delta\tau_{12}$ of different turbulence models at Re $= 2800$ with a grid resolution of 256×129 and $L_x = 9.0$: (a) SA model, (b) SST k-ω model, (c) GANN model, (d) LANN model, and (e) SLANN model.
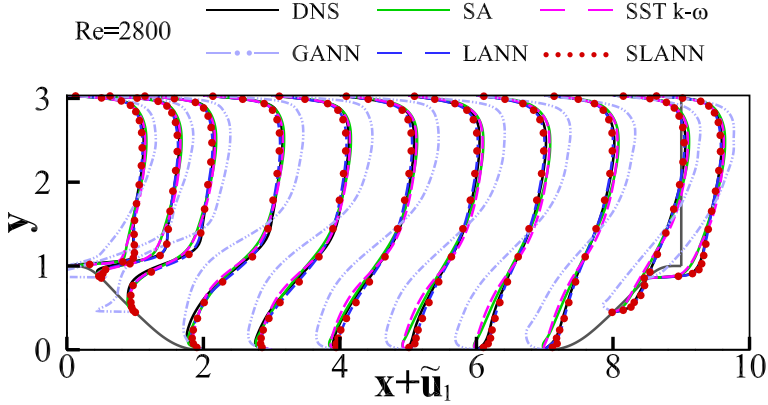
FIG. 12. Mean streamwise velocity $\tilde{u}_1$ profiles predicted by different turbulence models at Re = 2800 with a grid resolution of 256×129 and $L_x = 9.0$.

τ_{11}, τ_{12}, τ_{21}, τ_{22} (or Q_1, Q_2) simultaneously] models can predict the Reynolds stress and turbulent heat flux well, which are similar to the results of the DNS. In particular, although the magnitude of the turbulent heat flux is very small and can be ignored at this low-speed flow, it can be predicted by the GANN and LANN models well.

B. A posteriori tests

We evaluate the performance of the LANN model for flows over periodic hills with varying slopes at Re = 2800, 5600, 10 595, 19 000, and 37 000. Furthermore, in order to show that the LANN model can be applied to flows over periodic hills with varying slopes, *a posteriori* studies of the LANN model applied to flow over periodic hills with the total horizontal length of the domain $L_x = 3.858\alpha + 5.142$, where $\alpha = 1.5$, were conducted [71]. Here, α controls the width of the hill, and the length of the flat section between the hills is 5.142, which is kept constant. The two-dimensional Reynolds-averaged Navier-Stokes equations are solved with the finite volume solver OpenCFD-EC developed by Li *et al.* [72,73]. The spatial gradients are calculated with a second-order accurate discretization. The temporal advancement of the equations is achieved using an implicit lower-upper symmetric Gauss-Seidel (LU-SGS) method. The flow is set to be periodic
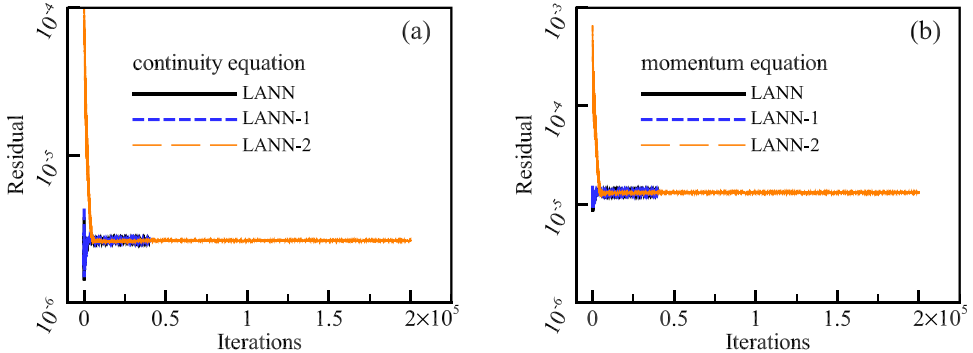

FIG. 13. The iteration of the rms residuals for the continuity and momentum equations for the LANN, LANN-1, and LANN-2 models at Re = 2800 with a grid resolution of 256×129 and $L_x = 9.0$: (a) continuity equation ($\bar{\rho}$) and (b) momentum equation ($\tilde{u}_1$).
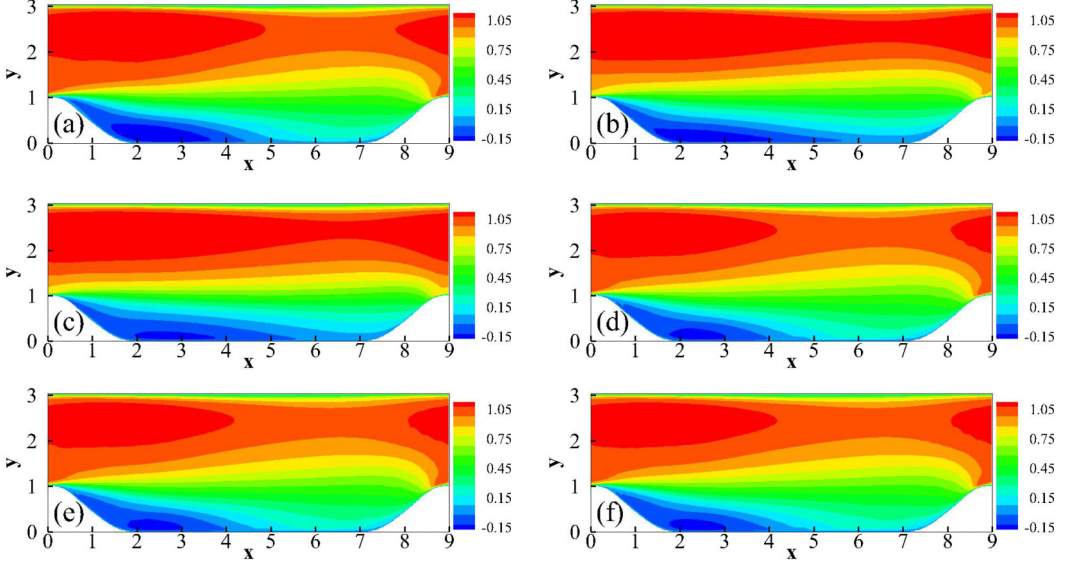
FIG. 14. The contours of the mean streamwise velocity $\tilde{u}_1$ of different turbulence models at Re = 2800 with a grid resolution of 256×129 and $L_x = 9.0$: (a) DNS, (b) SA model, (c) SST k-ω model, (d) LANN model, (e) LANN-1 model, and (f) LANN-2 model.

in the streamwise direction. No-slip and adiabatic conditions are set at walls for the velocity and temperature, respectively.

The SA model solves a transport equation for ν_t; the eddy viscosity can be calculated from

$$\mu_t = \rho \nu_t f_{v1}. \tag{20}$$

The governing equation for the intermediate variable ν_t is [7]

$$\frac{\partial \nu_t}{\partial t} + \frac{\partial}{\partial x_j}(\nu_t \tilde{u}_j) = c_{b1} S_t \nu_t + \frac{1}{\sigma}\left[\frac{\partial}{\partial x_j}\left((\tilde{\nu} + \nu_t)\frac{\partial \nu_t}{\partial x_j}\right) + c_{b2}\frac{\partial \nu_t}{\partial x_j}\frac{\partial \nu_t}{\partial x_j}\right] - c_{w1} f_w \left(\frac{\nu_t}{d}\right)^2, \tag{21}$$

where $S_t = \Omega + \frac{\nu_t}{k^2 d^2} f_{v2}$, $f_{v1} = \frac{\chi^3}{\chi^3 + c_{v1}^3}$, $f_{v2} = 1 - \frac{\chi}{1 + \chi/f_{v1}}$, $\chi = \frac{\rho \nu_t}{\mu}$, $f_w = g[\frac{1+C_{w3}^6}{g^6 + C_{w3}^6}]^{1/6}$, $g = r + C_{w2}(r^6 - r)$, $r = \frac{\nu_t}{S_t k^2 d^2}$, Ω is the magnitude of the vorticity vector, and d is the nearest distance from the walls. Meanwhile, the model coefficients in the SA model are $\sigma = 2/3$, $C_{b1} = 0.1355$, $C_{b2} = 0.622$, $\kappa = 0.41$, $C_{w1} = \frac{c_{b1}}{\kappa^2} + (1 + C_{b2})/\sigma$, $C_{w2} = 0.3$, $C_{w3} = 2$, $C_{v1} = 7.1$, and $C_{w1} = C_{b1}/k^2 + (1 + C_{b2})/\sigma$. The periodic boundary condition is applied in the streamwise x direction for ν_t. $\nu_t^{wall} = 0$ is imposed on the upper and lower wall boundaries.

The Menter SST k-ω model is a two-equation eddy-viscosity model, which has been widely used in the aerodynamic applications for its robustness and prediction of flow separation [12,74,75]. The eddy viscosity of the SST k-ω model is given by

$$\mu_t = \frac{a_1 \rho k}{\max(a_1 \omega, f_2 \omega)/\text{Re}}. \tag{22}$$

The governing equations for the turbulent kinetic energy k and specific dissipation rate ω are [12,74,75]

$$\frac{\partial \rho k}{\partial t} + \frac{\partial}{\partial x_j}(\rho k \tilde{u}_j) = \frac{1}{\text{Re}}\frac{\partial}{\partial x_j}\left[(\mu_L + \sigma_k \mu_T)\frac{\partial k}{\partial x_j}\right] + \frac{1}{\text{Re}}P_k - \text{Re}\beta^* \rho \omega k, \tag{23}$$
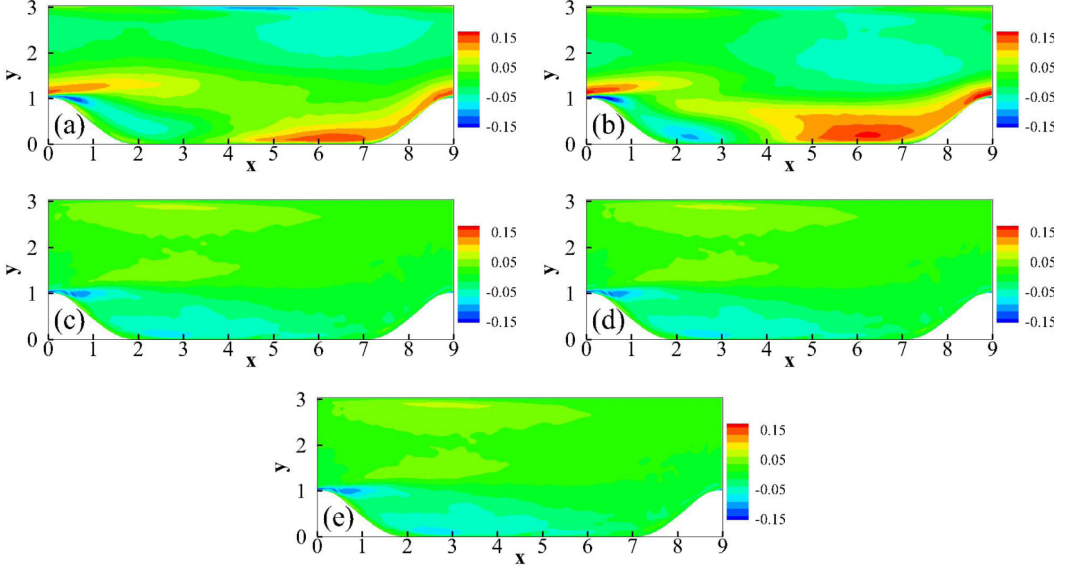
FIG. 15. The contours of the mean streamwise velocity error $\delta\tilde{u}_1$ of different turbulence models at Re $=$ 2800 with a grid resolution of 256×129 and $L_x = 9.0$: (a) SA model, (b) SST k-ω model, (c) LANN model, (d) LANN-1 model, and (e) LANN-2 model.

$$\frac{\partial \rho \omega}{\partial t} + \frac{\partial}{\partial x_j}(\rho \omega \tilde{u}_j) = \frac{1}{\mathrm{Re}} \frac{\partial}{\partial x_j}\left[(\mu_L + \sigma_\omega \mu_T)\frac{\partial \omega}{\partial x_j}\right] + \frac{1}{\mathrm{Re}}P_\omega - \frac{1}{\mathrm{Re}}2(1 - f_1)\frac{\rho \sigma_{\omega 2}}{\omega}\frac{\partial k}{\partial x_j}\frac{\partial \omega}{\partial x_j}, \quad (24)$$

where $P_k = \mu_t \Omega^2$, $P_\omega = C_\omega \rho \Omega^2$, $a_1 = 0.31$, and $\beta^* = 0.09$. The model coefficients σ_K, σ_ω, β, and C_ω in the SST k-ω model are obtained by blending the coefficients of the k-ω model (ϕ_1) with those of the transformed k-ϵ model (ϕ_2). The corresponding relation is $\phi = f_1\phi_1 + (1 - f_1)\phi_2$. The function f_1 is given by $f_1 = \tanh(\mathrm{arg}_1^4)$, $\mathrm{arg}_1 = \min[\max(\Gamma_1, \Gamma_3), \Gamma_2]$, $\Gamma_1 = \frac{1}{\mathrm{Re}^2}\frac{500\mu_L}{\rho\omega d^2}$, $\Gamma_2 = \frac{4\rho\sigma_{\omega 2}k}{CD_{K\omega}d^2}$, $\Gamma_3 = \frac{1}{\mathrm{Re}}\frac{\sqrt{k}}{0.09\omega d}$, $CD_{K\omega} = \max(2\frac{\rho\sigma_{\omega 2}}{\omega}\frac{\partial k}{\partial x_j}\frac{\partial \omega}{\partial x_j}, 10^{-20})$. The auxiliary function f_2 is defined as $f_2 = \tanh(\mathrm{arg}_2^2)$, where $\mathrm{arg}_2 = \max(2\Gamma_3, \Gamma_1)$. Meanwhile, the coefficients of the k-ω model are given by $\sigma_{K1} = 0.85$, $\sigma_{\omega 1} = 0.5$, $\beta_1 = 0.075$, and $C_{\omega 1} = 0.533$; the coefficients of the k-ϵ model are defined as $\sigma_{K2} = 1.0$, $\sigma_{\omega 2} = 0.856$, $\beta_2 = 0.0828$, and $C_{\omega 2} = 0.440$.
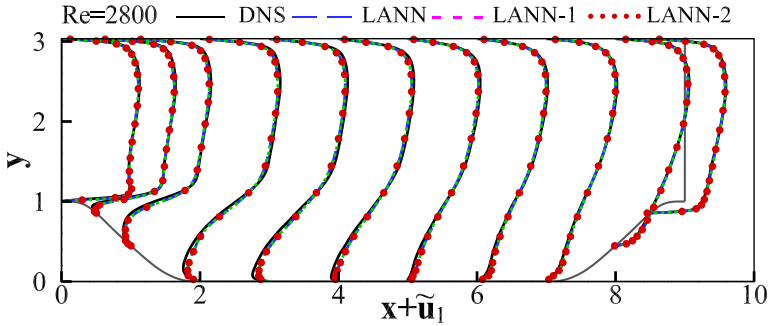

FIG. 16. Mean streamwise velocity $\tilde{u}_1$ profiles predicted by the LANN models with different initial conditions at Re $=$ 2800 with a grid resolution of 256×129 and $L_x = 9.0$.
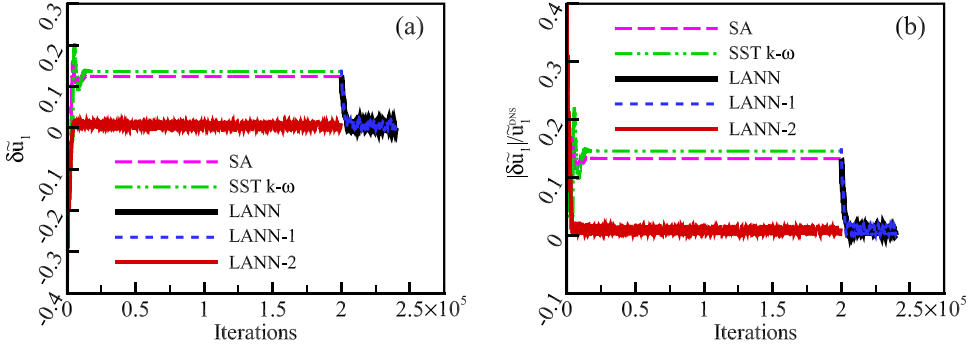
FIG. 17. The iteration of the mean velocity error at the point $(x, y) = (0.5, 1.2)$ for the SA, SST k-ω, LANN, LANN-1, and LANN-2 models at Re $= 2800$ with a grid resolution of 256×129 and $L_x = 9.0$: (a) $\delta\tilde{u}_1$ and (b) $|\delta\tilde{u}_1|/\tilde{u}_1^{\mathrm{DNS}}$.

Figures 10 and 11 show the Reynolds stress τ_{12} and its error $\delta\tau_{12}$ ($\delta\tau_{12} = \tau_{12}^{\mathrm{DNS}} - \tau_{12}^{\mathrm{model}}$) predicted by different turbulence models in the *a posteriori* test. Both the SA and SST k-ω models predict τ_{12} poorly. Meanwhile, τ_{12} predicted by the GANN model is much smaller than the result of the DNS near the lower wall. The LANN and SLANN models predict τ_{12} closer to the DNS. Furthermore, the mean streamwise velocity $\tilde{u}_1$ predicted by different turbulence models at 11 locations is shown in Fig. 12. The gray vertical line at $x = 9$ means the right boundary of the computational domain. The abscissa is $x + \tilde{u}_1$, which is plotted from zero to 10 to show the change of $x + \tilde{u}_1$. Due to numerical instability, the GANN model cannot predict the mean streamwise velocity $\tilde{u}_1$ well. Both the SA and SST k-ω models show similar characteristics. $\tilde{u}_1$ predicted by the SA and SST k-ω models are obviously smaller than that of the DNS data near the second hill. The LANN and SLANN models can accurately predict $\tilde{u}_1$ near the upper and lower walls, which are consistent with the results of Figs. 10 and 11.

In this research, the RANS solver with the SA model was employed to reach convergence, and the simulation with the LANN model was also performed to reach a convergent state. In order to study the impact of the initialization and the residual behavior of the LANN model, two more initializations are considered, which use the following fields as initial flow fields: (1) the convergent flow field with the SST k-ω model, and (2) $\bar{\rho} = 1.0$, $\tilde{u}_1 = 0.72$, and $\tilde{T} = 1.0$, which are abbreviated as the LANN-1 and LANN-2 models, respectively. The rms residuals of the RANS solver with different models are shown in Fig. 13, and they converge to less than 3×10^{-6} for the continuity equation ($\bar{\rho}$) and to less than 2×10^{-5} for the momentum equation ($\tilde{u}_1$) [22]. Furthermore, Figures 14 and 15 show the contours of the mean streamwise velocity $\tilde{u}_1$ and its error $\delta\tilde{u}_1 = \tilde{u}_1^{\mathrm{DNS}} - \tilde{u}_1^{\mathrm{model}}$ predicted by different turbulence models. The LANN models with different initial conditions show similar characteristics, which perform better than the SA and SST k-ω models. As shown in Figs. 16 and 12, the mean stream velocity profiles predicted
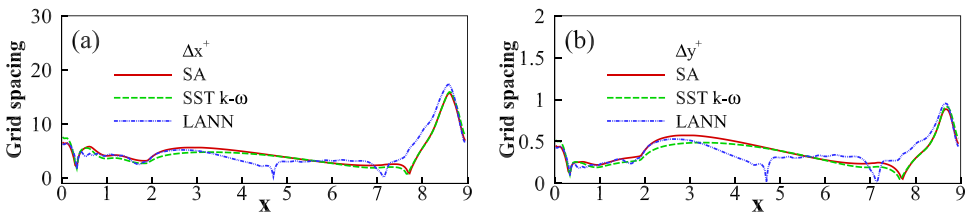

FIG. 18. Grid spacing in wall units along the bottom wall of RANS simulations with the SA, SST k-ω, and LANN models at Re $= 2800$ with a grid resolution of 256×129 and $L_x = 9.0$.
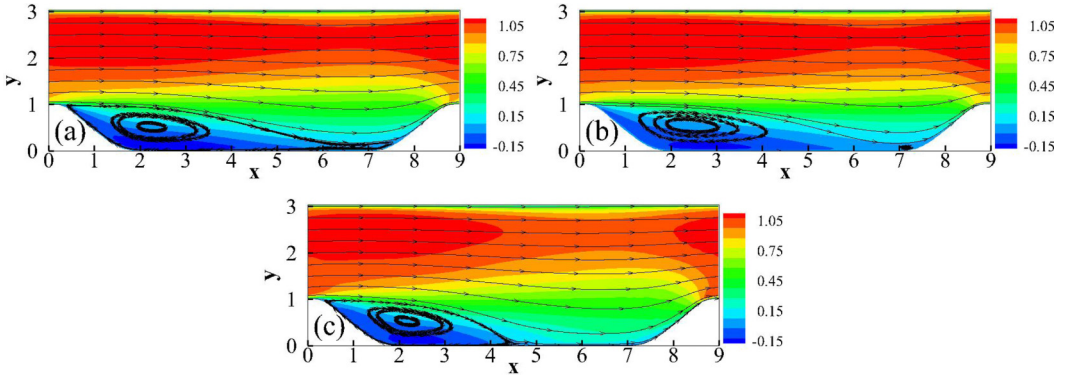
FIG. 19. Hill flow contours of the mean streamwise velocity $\tilde{u}$ and the streamlines at Re = 2800 with a grid resolution of 256×129 and $L_x = 9.0$: (a) SA model, (b) SST k-ω model, and (c) LANN model.

by the LANN models are closer to the DNS result than the SA and SST k-ω models. The iterative behavior of the velocity error $\delta\tilde{u}_1$ at the point $(x, y) = (0.5, 1.2)$ near the separation region is shown in Fig. 17. The velocity error $\delta\tilde{u}_1$ converges after the desired number of iterations, which implies that the RANS simulations are reasonable. The velocity error $\delta\tilde{u}_1$ predicted by the LANN models is one order of magnitude smaller than that predicted by the SA and SST k-ω models. These results show that the LANN models with different initialization are convergent and consistent.

Both *a priori* and *a posteriori* tests of the SLANN model and the LANN model are shown in Figs. 9–12. The predictions by the LANN model are similar to those of the SLANN model. Thus,
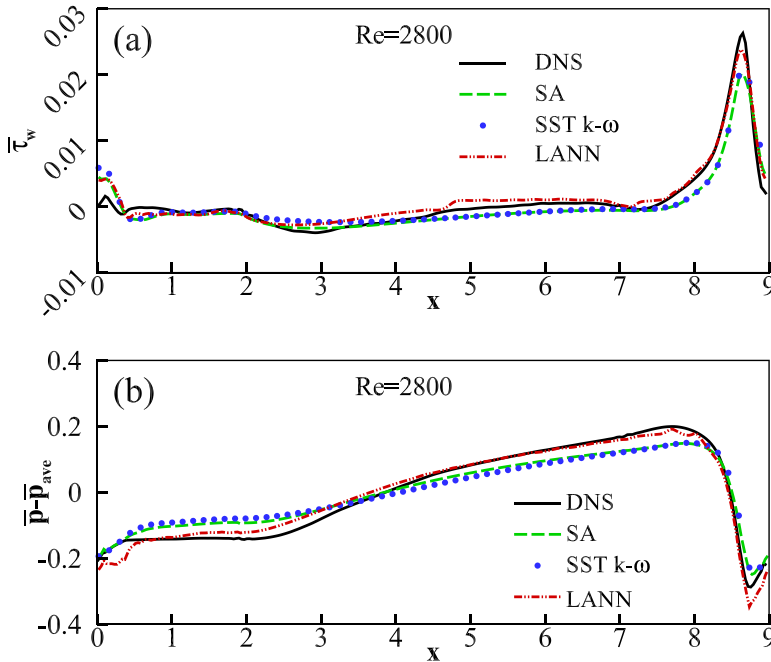

FIG. 20. Profiles of the averaged wall shear stress $\tilde{\tau}_w$ and the averaged pressure distribution $\bar{p}$ at Re = 2800 with a grid resolution of 256×129 and $L_x = 9.0$: (a) $\tilde{\tau}_w$ and (b) $\bar{p}$.
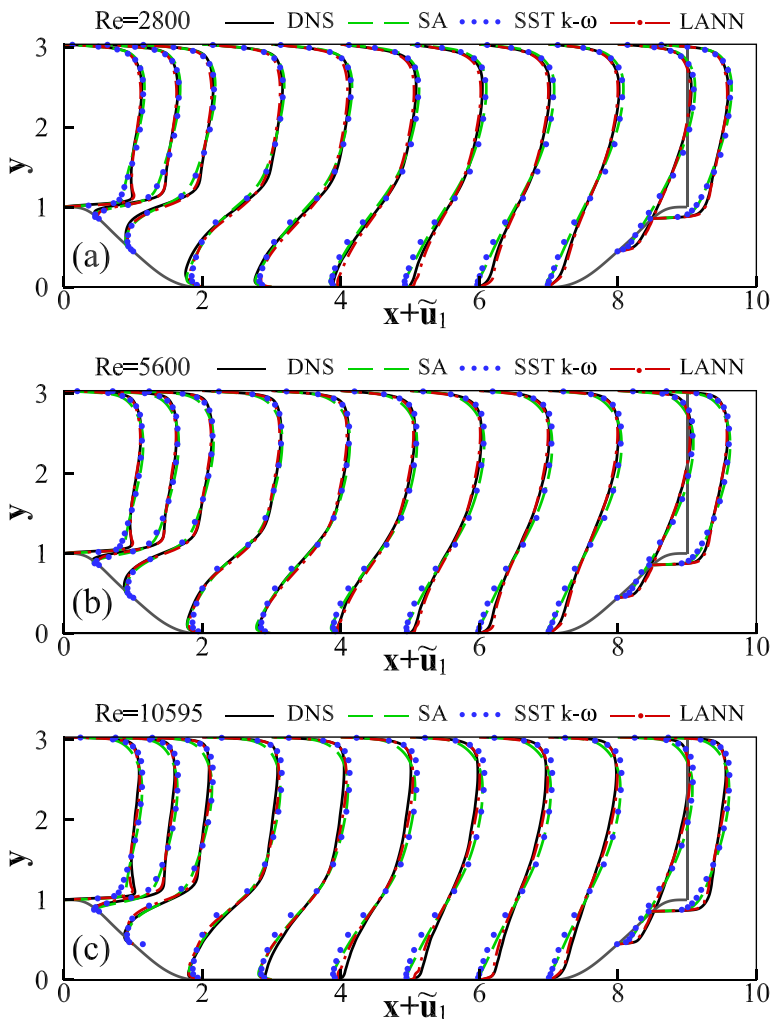
FIG. 21. Mean streamwise velocity $\tilde{u}_1$ profiles with a grid resolution of 256×129 and $L_x = 9.0$: (a) Re = 2800, (b) Re = 5600, and (c) Re = 10 595.

the LANN model can give reasonable results. Different from the work of Ling *et al.* by incorporating invariances into their relationship between velocity gradient and Reynolds stress [22], the impact of density, viscosity, and the nearest distance from the walls, d, are considered in this work, and it is hard to incorporate invariances directly into their relationship between inputs and outputs. We train τ_{ij} and Q_j separately where no physical constraint is added to the ANN training, although it is important to train all outputs simultaneously with some physical constraints to ensure the physical realizability of τ_{ij} and Q_j for the ANN model. We will focus on the ANN models with some physical constraints in the next step.

The performances of the LANN model are evaluated by calculating the average velocity, wall-shear stress, and average pressure. The variations of the grid spacing in wall units in the x and y directions along the bottom wall for RANS simulations with the SA, SST k-ω, and LANN models are shown in Fig. 18. The maximum grid spacings in the x and y directions are located at the downstream wall due to a large increase in the friction velocity in this region. Figure 19 shows the mean streamwise velocity contours and the streamlines from RANS simulations with the SA, SST

TABLE III. Relative error (E_r) of $\tilde{u}_1$ for different models at Re = 2800 and $y = 2.5$ with the grid resolution of 256×129.

$E_r \backslash x$	0	0.5	1	2	3	4	5	6	7	8	8.5
SA	0.035	0.030	0.026	0.020	0.026	0.039	0.054	0.061	0.061	0.050	0.044
SST k-ω	0.018	0.014	0.010	0.005	0.012	0.028	0.043	0.050	0.046	0.033	0.027
LANN	0.015	0.018	0.021	0.032	0.032	0.029	0.025	0.022	0.019	0.015	0.014

k-ω, and LANN models. The separation and reattachment points are at $x_{\text{sep}} = 0.316, 0.318, 0.346$ and $x_{\text{reatt}} = 7.70, 7.15, 4.80$ for the SA, SST k-ω, and LANN models, respectively. The separation point at $x_{\text{sep}} = 0.316$ predicted by the SA model is slightly closer to the DNS result ($x_{\text{sep}} = 0.227$). The reattachment point at $x_{\text{reatt}} = 4.80$ predicted by the LANN model is much closer to the DNS result ($x_{\text{reatt}} = 5.34$).

Figure 20(a) shows the distribution of the averaged wall shear stress $\tilde{\tau}_w$ along the lower wall at Re = 2800 ($\tilde{\tau}_w = \frac{1}{\text{Re}} \frac{\partial \tilde{u}_\xi}{\partial \eta}$, where $\tilde{u}_\xi$ is the flow velocity parallel to the wall and η is the distance to the wall). $\tilde{\tau}_w$ predicted by the LANN, SA, and SST k-ω models show similar behaviors as the DNS data. The peak of the profile of $\tilde{\tau}_w$ is recovered more accurately by the LANN model than the SA and SST k-ω models. The averaged pressure along the lower wall at Re = 2800 is shown in Fig. 20(b). The mean pressure predicted by the LANN model is closer to the DNS data than that predicted by the SA and SST k-ω models in the range $1 \leqslant x \leqslant 8$. We compare the mean streamwise velocity $\tilde{u}_1$ at 11 locations in Fig. 21. The SA, SST k-ω, and LANN models accurately predict $\tilde{u}_1$ near the upper wall. The RANS simulation with the SA and SST k-ω models do a poor job near the lower wall, especially behind the separation. In contrast, $\tilde{u}_1$ predicted by the RANS simulation with the LANN model are in good agreement with the DNS data at all locations, suggesting that the LANN model can predict the mean streamwise velocity $\tilde{u}_1$ of flows over periodic hills accurately. Furthermore, the performance of the LANN model trained at Re = 2800 is examined by predicting the mean streamwise velocity $\tilde{u}_1$ profile for flows over periodic hills with higher Reynolds numbers Re = 5600 and 10 595. We display the mean streamwise velocities $\tilde{u}_1$ of DNS and RANS simulations with the SA, SST k-ω, and LANN models at Re = 5600 and 10 595 in Figs. 21(b) and 21(c). One can see that some errors occur near the lower and upper walls in the predicted $\tilde{u}_1$ by the SA and SST k-ω models. In contrast, the results of the LANN model are very close to those of the DNS. Table III shows relative errors of $\tilde{u}_1$ for different models at Re = 2800 and $y = 2.5$. The relative errors of the LANN model are smaller than 0.03 for all the points.

The generality of the LANN model is examined by plotting the mean streamwise velocity $\tilde{u}_1$ profiles for flows over periodic hills on coarser grids and in a different computational domain (the detailed information about the new L_x can be given with $L_x = 3.858\alpha + 5.142$, where $\alpha = 1.5$) [71]. The mean streamwise velocity $\tilde{u}_1$ profiles for Re = 2800, 5600, and 10 595 with a grid resolution of 128×65 are shown in Fig. 22. Values of $\tilde{u}_1$ predicted by the LANN model are much closer to those of DNS, compared to those predicted by the SA and SST k-ω models. Furthermore, we evaluated the performance of the LANN model against the experimental results by Rapp *et al.* at Re = 19 000 and 37 000 [76]. As shown in Fig. 23, compared with the results from the experiments [76], the mean streamwise velocity $\tilde{u}_1$ from the LANN model matches better than those from the SA model. Finally, Fig. 24 shows the mean streamwise velocity $\tilde{u}_1$ for flow over periodic hills with a total horizontal length of $L_x = 10.929$ ($\alpha = 1.5$). The results from the LANN model show good agreement with the DNS results, which are better than those obtained with the SA and SST k-ω models under the same grid resolutions.
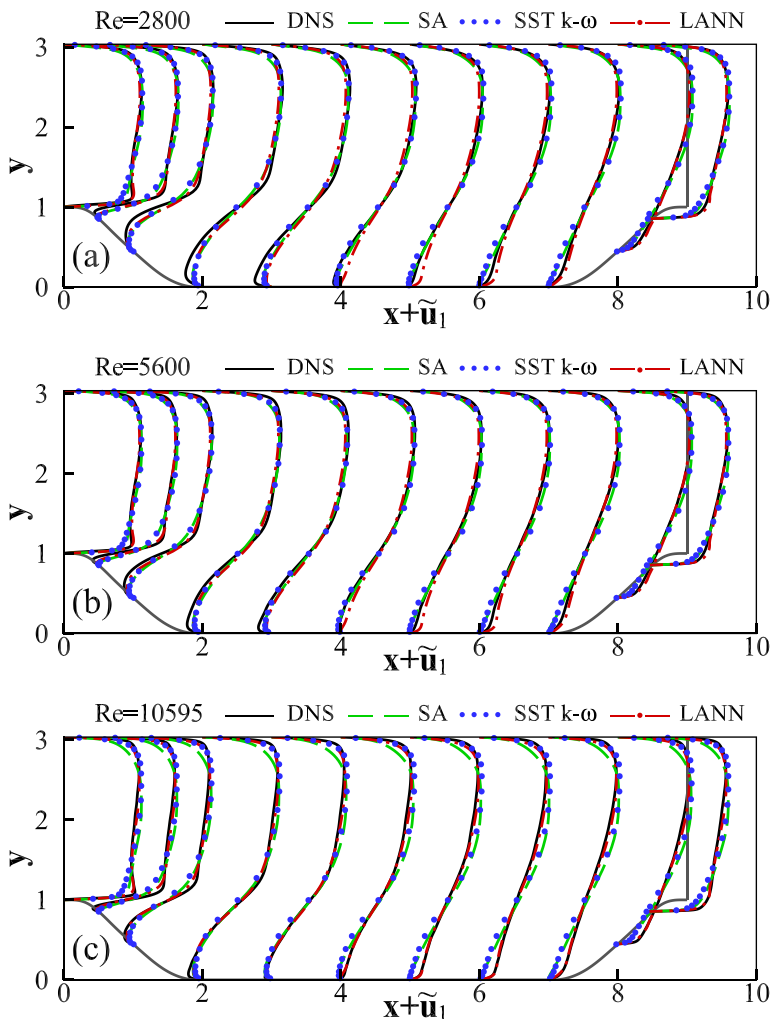
FIG. 22. Mean streamwise velocity $\tilde{u}_1$ profiles with a grid resolution of 128×65 and $L_x = 9.0$: (a) Re = 2800, (b) Re = 5600, and (c) Re = 10595.

VI. DISCUSSION

The flow over a periodic hill is one of the standard examples for developing new turbulence models of RANS [41], which includes the separation, recirculation, and reattachment. One important characteristic of RANS models is that the RANS unclosed terms are very complex in turbulence near the boundary. It is hard to reconstruct the RANS unclosed terms accurately and stably near a wall, which depend strongly on the distance to the walls [7,41]. Due to the irregular and diverse nature of turbulence, it is difficult to explicitly derive the dependence of RANS unclosed terms on the mean flow properties with analytical methods. The advantage of the LANN model in the local reference frame is that the η axis of the local coordinate system is orthogonal to the nearer wall and the nearest distance from the walls, d, can be measured along the coordinate axis η, which is general and versatile for complex wall conditions. In this research, it has been demonstrated that the LANN method is a powerful tool which can efficiently learn the high-dimensional and nonlinear relations between the RANS unclosed terms and the mean flow fields for flows over periodic hills with varying slopes. In this work, the Reynolds stress and turbulence heat flux are trained without
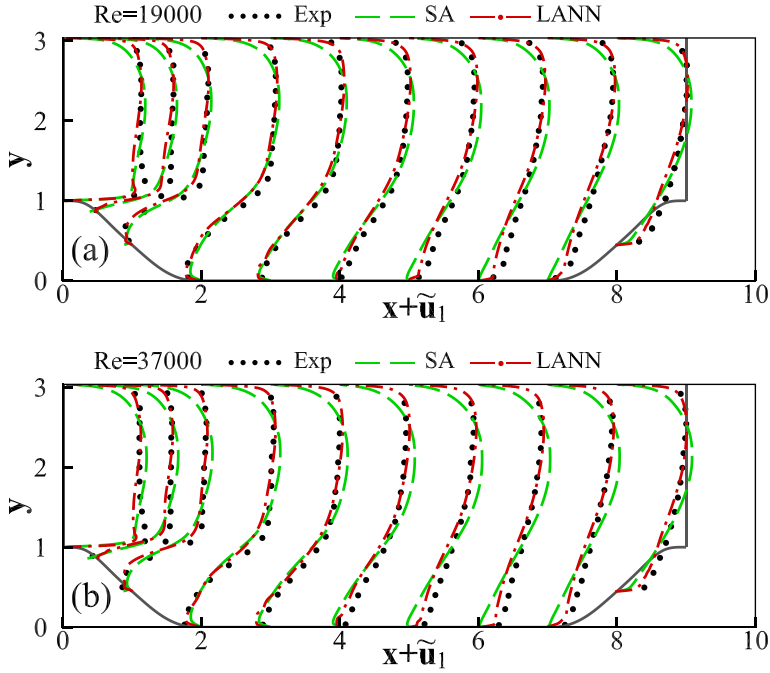
FIG. 23. Mean streamwise velocity $\tilde{u}_1$ profiles with a grid resolution of 256×129 and $L_x = 9.0$; dotted curves denotes experiments of Rapp and Manhart [76]: (a) Re = 19 000 and (b) Re = 37 000.
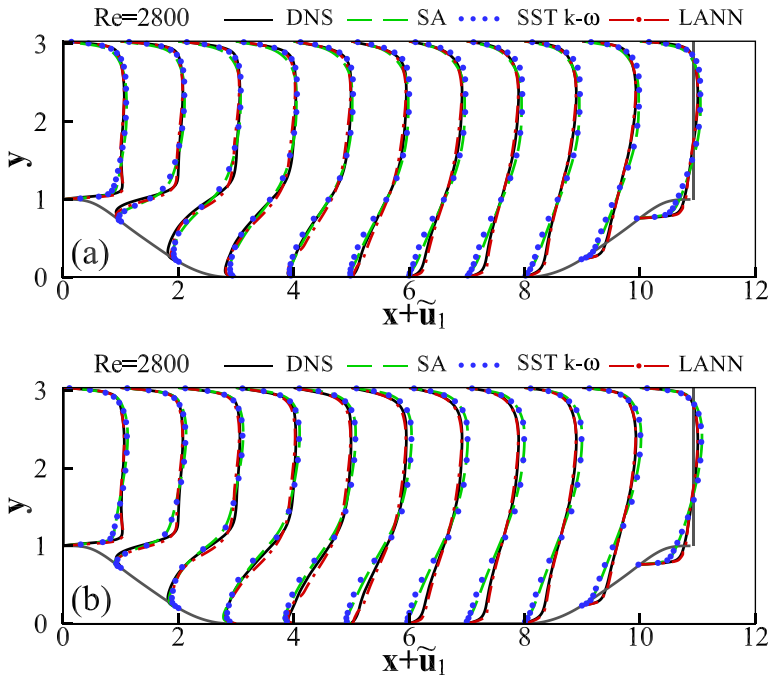

FIG. 24. Mean streamwise velocity $\tilde{u}_1$ profiles at Re = 2800 with $L_x = 10.929$ ($\alpha = 1.5$): (a) grid resolution of 128×65 and (b) grid resolution of 256×129.

guaranteeing the symmetric and Galilean invariant. It is important to train all components with symmetric properties and physical realizability for future ANN models. We will follow the works of Pope and Ling *et al.* to incorporate invariances into the relationship between velocity gradient and Reynolds stress in the local reference frame [22,77]. The effects of more complex boundary conditions on the RANS simulations of wall-bounded turbulent flows will be modeled with the LANN framework in a follow-up study.

VII. CONCLUSIONS

In this work, we proposed a framework of LANN for the RANS unclosed terms in RANS simulations of compressible turbulence. The proposed LANN model depends on the local coordinate system orthogonal to the wall for flows over periodic hills. In the *a priori* test, the correlation coefficients are larger than 0.96 and the relative errors are smaller than 18% for the LANN model. In an *a posteriori* analysis, we compare the performances of the LANN model with those of the GANN, SA, and SST k-ω models in the predictions of the average velocity, wall-shear stress, and average pressure in flows over periodic hills with varying slopes $\alpha = 1$ and 1.5. There are non-negligible errors between the mean velocities predicted by the GANN, SA, and SST k-ω models and the results of DNS near the walls, especially in the region right behind the separation. In contrast, the LANN model predicts the mean velocity accurately, and it also reconstructs the mean pressure closer to those of the DNS than those with the SA and SST k-ω models at Reynolds numbers Re = 2800, 5600, 10 595, 19 000, and 37 000. In addition, the mean velocity in flows over periodic hills with longer horizontal width $L_x = 10.929$ ($\alpha = 1.5$) predicted by the LANN model is in well agreement with that of the DNS. The above comparison showed that the LANN model outperformed the GANN, SA, and SST k-ω models in the flows over periodic hills.

The LANN model should also be very useful to wall-bounded turbulent flows with curved walls. There are several issues that need further exploration: the physical relationship between averaged flow fields and the RANS unclosed terms, the hyperparameter space, the symmetry and interpretation of the neural network models, the nonlocality characteristics of the RANS dynamics, and applications in more complex flows.

ACKNOWLEDGMENTS

[1] C. G. Speziale, Analytical methods for the development of Reynolds-stress closures in turbulence, Annu. Rev. Fluid Mech. **23**, 107 (1991).

[2] S. B. Pope, *Turbulent Flows* (Cambridge University Press, Cambridge, U.K., 2000).

[3] P. A. Durbin, Some recent developments in turbulence closure modeling, Annu. Rev. Fluid Mech. **50**, 77 (2018).

[4] O. Reynolds, On the dynamical theory of incompressible viscous fluids and the determination of the criterion, Philos. Trans. R. Soc. London A **186**, 123 (1895).

[5] J. Boussinesq, Mem. Théorie de l'écoulement tourbillant, Mem. Présentés par Divers Savants Acad. Sci. Inst. Fr. **23**, 46 (1877).

[6] L. Prandtl, Über die ausgebildete Turbulenz, Z. Angew. Math. Mech. **5**, 136 (1925).

[7] P. R. Spalart and S. R. Allmaras, A one-equation turbulence model for aerodynamic flows, in *Proceedings of the 30th AIAA Aerospace Sciences Meeting and Exhibit, Reno, NV*, AIAA Paper No. 1992-439 (AIAA, 1992).

[8] W. P. Jones and B. E. Launder, The prediction of laminarization with a two-equation model of turbulence, Int. J. Heat Mass Transfer **15**, 301 (1972).

[9] B. E. Launder and B. I. Sharma, Application of the energy dissipation model of turbulence to the calculation of flow near a spinning disc, Lett. Heat Mass Transf. **1**, 131 (1974).

[10] V. Yakhot and S. A. Orszag, Renormalization group analysis of turbulence. I. Basic theory, J. Sci. Comput. **1**, 3 (1986).

[11] V. Yakhot, S. A. Orszag, S. Thangam, T. B. Gatski, and C. G. Speziale, Development of turbulence models for shear flows by a double expansion technique, Phys. Fluids A Fluid Dyn. **4**, 1510 (1992).

[12] F. R. Menter, Two-equation eddy-viscosity turbulence models for engineering applications, AIAA J. **32**, 1598 (1994).

[13] P. R. Spalart, Strategies for turbulence modeling and simulations, Int. J. Heat Fluid Flow **21**, 252 (2000).

[14] D. C. Wilcox, Formulation of the k-ω turbulence model revisited, AIAA J. **46**, 2823 (2008).

[15] B. E. Launder, G. J. Reece, and W. Rodi, Progress in the development of a Reynolds-stress turbulent closure, J. Fluid Mech. **68**, 537 (1975).

[16] B. Tracey, K. Duraisamy, and J. Alonso, Application of supervised learning to quantify uncertainties in turbulence and combustion modeling, in *Proceedings of the 51st AIAA Aerospace Sciences Meeting, Including the New Horizons Forum and Aerospace Exposition, Grapevine, TX*, AIAA Paper No. 2013-0259 (AIAA, Reston, VA, 2013).

[17] K. Duraisamy, Z. J. Zhang, and A. P. Singh, New approaches in turbulence and transition modeling using data-driven techniques, in *Proceedings of the 53rd AIAA Aerospace Sciences Meeting, Kissimmee, FL*, AIAA Paper No. 2015-1284 (AIAA, Reston, VA, 2015).

[18] E. J. Parish and K. Duraisamy, A paradigm for data-driven predictive modeling using field inversion and machine learning, J. Comput. Phys. **305**, 758 (2016).

[19] J. Weatheritt and R. Sandberg, A novel evolutionary algorithm applied to algebraic modifications of the RANS stress-strain relationship, J. Comput. Phys. **325**, 22 (2016).

[20] J. Ling and J. Templeton, Evaluation of machine learning algorithms for prediction of regions of high Reynolds averaged Navier Stokes uncertainty, Phys. Fluids **27**, 085103 (2015).

[21] Z. J. Zhang and K. Duraisamy, Machine learning methods for data-driven turbulence modeling, in *Proceedings of the 22nd AIAA Computational Fluid Dynamics Conference Dallas*, AIAA Paper No. 2015-2460 (AIAA, Reston, VA, 2015).

[22] J. Ling, A. Kurzawski, and J. Templeton, Reynolds averaged turbulence modelling using deep neural networks with embedded invariance, J. Fluid Mech. **807**, 155 (2016).

[23] J. Ling, R. Jones, and J. Templeton, Machine learning strategies for systems with invariance properties, J. Comput. Phys. **318**, 22 (2016).

[24] H. Xiao, J. L. Wu, J. X. Wang, J. X. Sun, and C. J. R. Roy, Quantifying and reducing model-form uncertainties in Reynolds-averaged Navier-Stokes simulations: A data-driven, physics-informed Bayesian approach, J. Comput. Phys. **324**, 115 (2016).

[25] B. D. Tracey, K. Duraisamy, and J. J. Alonso, A machine learning strategy to assist turbulence model development, in *Proceedings of the 53rd AIAA Aerospace Sciences Meeting, Kissimmee, FL*, AIAA Paper No. 2015-1287 (AIAA, Reston, VA, 2015).

[26] S. L. Brunton, J. L. Proctor, and J. N. Kutz, Discovering governing equations from data by sparse identification of nonlinear dynamical systems, Proc. Natl. Acad. Sci. USA **113**, 3932 (2016).

[27] J. X. Wang, J. L. Wu, and H. Xiao, Physics-informed machine learning approach for reconstructing Reynolds stress modeling discrepancies based on DNS data, Phys. Rev. Fluids **2**, 034603 (2017).

[28] A. P. Singh, K. Duraisamy, and Z. J. Zhang, Augmentation of turbulence models using field inversion and machine learning, in *Proceedings of the 55th AIAA Aerospace Sciences Meeting, Grapevine, TX*, AIAA Paper No. 2017-0993 (AIAA 2017).

[29] J. N. Kutz, Deep learning in fluid dynamics, J. Fluid Mech. **814**, 1 (2017).

[30] A. Vollant, G. Balarac, and C. Corre, Subgrid-scale scalar flux modelling based on optimal estimation theory and machine-learning procedures, J. Turbul. **18**, 854 (2017).

[31] A. T. Mohan and D. V. Gaitonde, A deep learning based approach to reduced order modeling for turbulent flow control using LSTM neural networks, arXiv:1804.09269.

[32] M. Raissi and G. E. Karniadakis, Hidden physics models: Machine learning of nonlinear partial differential equations, J. Comput. Phys. **357**, 125 (2018).

[33] J. L. Wu, H. Xiao, and E. Paterson, Physics-informed machine learning approach for augmenting turbulence models: A comprehensive framework, Phys. Rev. Fluids **3**, 074602 (2018).

[34] L. Jofre, S. P. Domino, and G. Iaccarino, A framework for characterizing structural uncertainty in large-eddy simulation closures, Fluid Turbul. Combust. **100**, 341 (2018).

[35] C. Ma, J. Wang, and W. E, Model reduction with memory and the machine learning of dynamical systems, Commun. Comput. Phys. **25**, 947 (2019).

[36] J. L. Wu, H. Xiao, R. Sun, and Q. Q. Wang, Reynolds-averaged Navier-Stokes equations with explicit data-driven Reynolds stress closure can be ill-conditioned, J. Fluid Mech. **869**, 553 (2019).

[37] L. Y. Zhu, W. W. Zhang, J. Q. Kou, and Y. L. Liu, Machine learning methods for turbulence modeling in subsonic flows around airfoils, Phys. Fluids **31**, 015105 (2010).

[38] C. Y. Xie, J. C. Wang, K. Li, and C. Ma, Artificial neural network approach to large-eddy simulation of compressible isotropic turbulence, Phys. Rev. E **99**, 053113 (2019).

[39] C. Y. Xie, K. Li, C. Ma, and J. C. Wang, Modeling subgrid-scale force and divergence of heat flux of compressible isotropic turbulence by artificial neural network, Phys. Rev. Fluids **4**, 104605 (2019).

[40] C. Y. Xie, J. C. Wang, H. Li, M. P. Wan, and S. Y. Chen, Artificial neural network mixed model for large eddy simulation of compressible isotropic turbulence, Phys. Fluids **31**, 085112 (2019).

[41] K. Duraisamy, G. Iaccarino, and H. Xiao, Turbulence modeling in the age of data, Annu. Rev. Fluid Mech. **51**, 357 (2019).

[42] R. Fang, D. Sondak, P. Protopapas, and S. Succi, Neural network models for the anisotropic Reynolds stress tensor in turbulent channel flow, J. Turbul. **21**, 525 (2020).

[43] S. Pandey, J. Schumacher, and K. R. Sreenivasan, A perspective on machine learning in turbulent flows, J. Turbul. **21**, 567 (2020).

[44] K. Duraisamy, Perspectives on machine learning-augmented Reynolds-averaged and large eddy simulation models of turbulence, Phys. Rev. Fluids **6**, 050504 (2021).

[45] S. Pawar, O. San, B. Aksoylu, A. Rasheed, and T. Kvamsdal, Physics guided machine learning using simplified theories, Phys. Fluids **33**, 011701 (2021).

[46] S. Beetham and J. Capecelatro, Formulating turbulence closures using sparse regression with embedded form invariance, Phys. Rev. Fluids **5**, 084611 (2020).

[47] R. Samtaney, D. I. Pullin, and B. Kosović, Direct numerical simulation of decaying compressible turbulence and shocklet statistics, Phys. Fluids **13**, 1415 (2001).

[48] X. L. Li, D. X. Fu, and Y. W. Ma, Direct numerical simulation of compressible turbulent flows, Acta. Mech. Sin. **26**, 795 (2010).

[49] J. Wang, Y. Shi, L.-P. Wang, Z. Xiao, X. T. He, and S. Chen, Effect of compressibility on the small scale structures in isotropic turbulence, J. Fluid Mech. **713**, 588 (2012).

[50] P. Balakumar, DNS/LES simulations of separated flows at high Reynolds numbers, in *Proceedings of the 45th AIAA Fluid Dynamics Conference, Dallas, TX*, AIAA Paper No. 2015-2783 (AIAA, 2015).

[51] X. Gloerfelt and P. Cinnella, Investigation of the flow dynamics in a channel constricted by periodic hills, in *Proceedings of the 45th AIAA Fluid Dynamics Conference, Dallas, TX*, AIAA Paper No. 2015-2480 (AIAA, 2015).

[52] W. Sutherland, The viscosity of gases and molecular force, Philos. Mag. S5 **36**, 507 (1992).

[53] A. Favre, Equations des gaz turbulents compressible. I. Formes generales, J. Mec. **4**, 361 (1965).

[54] Z. Jiang, Z. L. Xiao, Y. P. Shi, and S. Y. Chen, Constrained large-eddy simulation of wall-bounded compressible turbulent flows, Phys. Fluids **25**, 106102 (2013).

[55] Z. H. Xia, Y. P. Shi, R. K. Hong, Z. L. Xiao, and S. Y. Chen, Constrained large-eddy simulation of separated flow in a channel with streamwise-periodic constrictions, J. Turbul. **14**, 1 (2013).

[56] C. P. Mellen, J. Fröhlich, and W. Rodi, Large-eddy simulation of the flow over periodic hills, edited by M. Deville and R. Owens, in *Proceedings of the 16th IMACS World Congress, Lausanne, Switzerland, New Brunswick, N.J.* (2000).

[57] J. Frohlich, C. P. Mellen, W. Rodi, L. Temmerman, and M. A. Leschziner, Highly resolved large-eddy simulation of separated flow in a channel with streamwise periodic constraint, J. Fluid Mech. **526**, 19 (2005).

[58] D. X. Fu, Y. W. Ma, X. L. Li, and Q. Wang, *Direct Numerical Simulation of Compressible Turbulence* (Science Press, Beijing, 2010).

[59] S. K. Lele, Compact finite difference schemes with spectral-like resolution, J. Comput. Phys. **103**, 16 (1992).

[60] S. Obayashi, K. Matsushima, K. Fujii, and K. Kuwahara, Improvements in efficiency and reliability for Navier-Stokes computations using the LU-ADI factorization algorithm, in *Proceedings of the 24th AIAA Aerospace Sciences Meeting, Reno, NV*, AIAA Paper No. 1986-338 (1986).

[61] J. Ziefle, S. Stolz, and L. Kleiser, Large-eddy simulation of separated flow in a channel with streamwise-periodic constrictions, AIAA J. **46**, 1705 (2008).

[62] M. Breuer, N. Peller, C. Rapp, and M. Manhart, Flow over periodic hills–Numerical and experimental study in a wide range of Reynolds numbers, Comput. Fluids **38**, 433 (2009).

[63] X. Ge, O. V. Vasilyev, and M. Y. Hussaini, Wavelet-based adaptive delayed detached eddy simulations for wall-bounded compressible turbulent flows, J. Fluid Mech. **873**, 1116 (2019).

[64] M. Gamahara and Y. Hattori, Searching for turbulence models by artificial neural network, Phys. Rev. Fluids **2**, 054604 (2017).

[65] R. Maulik, H. Sharma, S. Patel, B. Lusch, and E. Jennings, A turbulent eddy-viscosity surrogate modeling framework for Reynolds-averaged Navier-Stokes simulations, Computers Fluids, **227**, 104777 (2021).

[66] C. Xie, J. Wang, and W. E, Modeling subgrid-scale forces by spatial artificial neural networks in large eddy simulation of turbulence, Phys. Rev. Fluids **5**, 054606 (2020).

[67] G. Zhang, B. E. Patuwo, and M. Y. Hu, Forecasting with artificial neural networks: The state of the art, Int. J. Forecast. **14**, 35 (1998).

[68] H. B. Demuth, M. H. Beale, O. D. Jess, and M. T. Hagan, *Neural Network Design* (Martin Hagan, Stillwater, OK, 2014).

[69] R. Maulik and O. San, A neural network approach for the blind deconvolution of turbulent flows, J. Fluid Mech. **831**, 151 (2017).

[70] D. P. Kingma and J. Ba, Adam: A method for stochastic optimization, arXiv:1412.6980.

[71] H. Xiao, J. L. Wu, S. Laizet, and L. Duan, Flows over periodic hills of parameterized geometries: A dataset for data-driven turbulence modeling from direct simulations, Comput. Fluids **200**, 104431 (2020).

[72] H. Gao, D. X. Fu, Y. W. Ma, and X. L. Li, Direct numerical simulation of supersonic boundary layer flow, Chin. Phys. Lett. **22**, 1709 (2005).

[73] X. L. Li, D. X. Fu, and Y. W. Ma, DNS of compressible turbulent boundary layer over a blunt wedge, Sci. China Ser. G. **48**, 129 (2005).

[74] F. R. Menter, Zonal two equation k-ω turbulence models for aerodynamic flows, in *Proceedings of the 23rd Fluid Dynamics, Plasmadynamics, and Lasers Conference, Orlando,FL*, AIAA Paper No. 1993-2906 (AIAA, 1993).

[75] J. Blazek, *Computational Fluid Dynamics: Principles and Applications*, 2nd ed. (Elsevier, Amsterdam, 2005).

[76] C. Rapp and M. Manhart, Flow over periodic hills: An experimental study, Exp. Fluids **51**, 247 (2011).

[77] S. B. Pope, A more general effective-viscosity hypothesis, J. Fluid Mech. **72**, 331 (1975).